Exp Fluids (2013) 54:1416
DOI 10.1007/s00348-012-1416-z

RESEARCH ARTICLE

3D Velocimetry and droplet sizing in the Ranque–Hilsch vortex tube

R. Liew · J. C. H. Zeegers · J. G. M. Kuerten · W. R. Michałek

Received: 26 June 2012 / Revised: 24 September 2012 / Accepted: 15 October 2012 / Published online: 20 December 2012

Abstract The Ranque–Hilsch vortex tube (RHVT) is a device currently used to generate local cooling. In general, the fluid that is injected into the RHVT is a single-phase gas. In this study, however, we have added a dispersed phase (water droplets) to the gas (nitrogen). By means of phase Doppler particle analysis, three velocity components, their higher order moments, and sizes of droplets were measured, showing high intensity velocity fluctuations in the core region of the main vortex. The frequency spectrum of the velocity is presented and reveals that wobbling of the vortex axis is the cause of the high intensity fluctuations. The wobbling motion reduces the influence of the droplet size on the radial droplet velocity.

1 Introduction

The vortex tube, as shown in Fig. 1, is a device that is used to generate (spot-) cooling, for example, for the machining of plastics and to cool electronic controls (Exair 2012; ITW-Vortec 2012; AirTx 2012). Simplicity, durability, no moving parts, its small size, and cold air that is instantly available make the vortex tube popular at places where pressurized air is at the disposal to generate low-cost cooling. The cooling effect by tangentially injecting pressurized gas into a cylindrical tube, from which the gas is allowed to escape from both ends, was first discovered by Ranque (1933) and improved by Hilsch (1947). Therefore, the vortex tube is often called the Ranque–Hilsch vortex tube (RHVT).

Since its invention, many scientists have focused on the energy separation process in the RHVT (Liew et al. 2012; Ahlborn et al. 1994; Gutsol 1997; Aljuwayhel et al. 2005; Gao 2005; Eiamsa-ard and Promvonge 2008; Deissler and Perlmutter 1960) or tried to increase its efficiency by optimizing the geometry of the vortex tube (Takahama and Yokosawa 1981; Nimbalkar and Muller 2009). Less attention was paid, however, to a second possible use for the RHVT: removal of non-desired condensable components from a gas stream. The high swirl velocity, the cooling effect, and the simplicity of the design make the RHVT suitable for the removal of water and carbon dioxide from natural gas.

The swirl velocity of the gas near the entrance of the RHVT is able to reach the speed of sound, resulting in an extremely large centrifugal acceleration. For example, values of the centrifugal acceleration of more than 10^6 m/s^2 are easily reached in a RHVT that has an inner diameter of 1 cm. The centrifugal acceleration is well suited, as in a cyclone separator, for separating the condensable components, which are in the form of small liquid droplets, from the gas stream. An additional advantage of the RHVT is the additional cooling effect, which can be used to liquify condensable components such as CO_2.

To investigate how droplets behave in the RHVT, we introduce small water droplets in the gas from which we have measured the velocities, higher order moments, and

R. Liew (✉) · J. C. H. Zeegers
Department of Applied Physics, Eindhoven University of Technology, P.O. Box 513, 5600 MB Eindhoven, The Netherlands
e-mail: r.liew@tue.nl

J. G. M. Kuerten
Faculty EEMCS, University of Twente, P.O. Box 217, 7500 AE Enschede, The Netherlands

J. G. M. Kuerten · W. R. Michałek
Department of Mechanical Engineering, Eindhoven University of Technology, P.O. Box 513, 5600 MB Eindhoven, The Netherlands

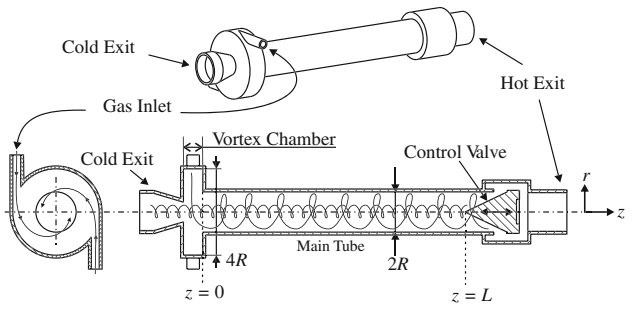

Fig. 1 Ranque–Hilsch vortex tube. R and L are the vortex tube radius and length, respectively; r and z are the radial and axial coordinates, respectively

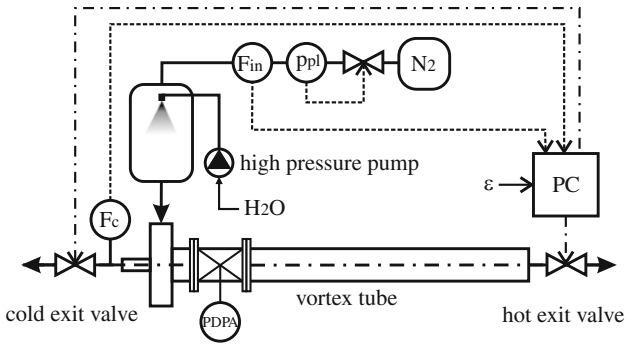

Fig. 2 Schematic overview of the experimental setup as used in the experiments

sizes by means of phase Doppler particle analysis. This paper presents results and analysis of this experimental study. The results of the experiments give important insight into the behavior of droplets as well as the behavior of the gas.

2 Methods and apparatus

Laser Doppler anemometry (LDA) is a well-established method that provides the velocity of seeding particles (Albrecht 2003). It uses at least two laser beams that intersect each other under an angle. If a seeding particle moves through the volume where the laser beams are crossing (which is the measurement volume), it scatters light in all directions. The intensity of the scattered light fluctuates in time due to interference of laser light on the particle and is detected by a sensor. The frequency of the detected signal is determined and used to compute the particle velocity in one direction. To be able to determine all three velocity components, three sets of beam pairs under different angles and/or planes are required.

Phase Doppler particle analysis (PDPA) is an extension for LDA that was used in this study and additionally provides droplet sizes. Scattered light from a droplet is detected by several sensors located at different positions relative to the measurement volume. Each sensor records a signal (the same as the signal obtained with regular LDA) from which the velocity can be deduced. Because of the positioning of the sensors, there exists a phase difference between the recorded signals that is used to determine the size of the droplet (Bachalo and Houser 1984).

A schematic overview of the experimental setup is shown in Fig. 2. Nitrogen gas was used as working fluid, and the plenum pressure p_{pl} was controlled via a pressure controller connected to the nitrogen tank N_2. During an experiment, the plenum pressure was kept constant. The ratio of the cold and inlet mass flow is the so-called cold fraction, $\varepsilon = \dot{m}_c/\dot{m}$, where $\dot{m}_c$ is the amount of gas leaving the device via the cold exit and $\dot{m}$ is the inlet mass flow. The inlet mass flow was measured via mass flow sensor F_{in} and was used together with the cold mass flow sensor F_c to regulate two exit valves, obtaining the set point value for ε while keeping $\dot{m}$ constant. The standard deviation of both flow meters used (Bronkhorst F-116AI-HAD-00-V) was <1 %.

2.1 The vortex tube

An RHVT consists of a cylindrical tube that is connected to a vortex chamber, shown in Fig. 1, to which several entrance nozzles are tangentially attached. Pressurized gas is expanded through the nozzles to generate a highly swirling motion—the vortex. Because of radial motions of gas in the tube, in combination with an existing pressure gradient due to rotation, energy is transported from the core toward the peripheral region (Liew et al. 2012; Deissler and Perlmutter 1960). Because of the energy transport, the core region cools down, while the peripheral region heats up.

The RHVT that was used in the experiments had an inner diameter of $2R = 40$ mm and a length of $L = 2.00$ m. The vortex chamber (Fig. 1) had a diameter of 80 mm and contained 8 rectangular slot nozzles with dimensions 1×14 mm. The cold exit was a hole in the vortex chamber that had a diameter of 15 mm.

2.2 PDPA configuration

The 3D PDPA system (TSI Inc. 2012) consisted, among others, of a FSA4000 multibit digital burst correlator, a continuous wave argon ion laser (Spectra-Physics Stabilite 2017, 7W power output), a 2D transceiver probe (TR260 for wavelengths 514.5 and 488 nm), and a 1D transceiver probe (TR160 for wavelength 476.5 nm). A receiver probe (RV2070) was used to determine the droplet size. The PDPA equipment was calibrated by TSI to have an accuracy of 3 % for droplets smaller than 10 μm. For larger

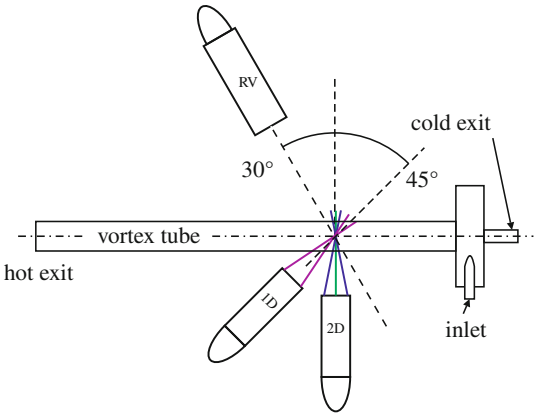

Fig. 3 Layout (*top view*) of the configuration of the fiber optic probes (1D and 2D) and the receiver probe (RV) with respect to the vortex tube

droplets, the uncertainty was 0.5 %. The optical configuration of the PDPA setup is shown in Fig. 3. The fiber optic probes and the receiver were mounted on a traverse system that had a positioning accuracy of 10 μm. All data were collected by FlowSizer^{TM} software.

2.3 Optical accessibility

The PDPA measurements were performed in a transparent section of the cylindrical tube of the RHVT. The section was partly fabricated from transparent plastic (polymethyl methacrylate or PMMA) and provided an optically accessible domain.

To be able to determine shear stresses of the fluid and droplet velocities, it is required that the velocity components are obtained from a single droplet, what can only be achieved if there is overlap of the three measurement volumes. The position of the measurement volumes was adjusted by moving the transmitting and receiving probes with a traverse system. Due to refraction of the laser beams through the cylindrical windows and the non-matching refractive indices of PMMA and nitrogen gas, the overlap of the measurement volumes varied with the radial position inside the RHVT, called astigmatism (Zhang and Eisele 1996, 1998; Zhang 2004). Refraction of the 514.5 nm laser beams through the curved window also made the beam crossing angle to change with r.

The thickness of the window material has a major influence on the astigmatism and measurement uncertainties. The minimum window thickness is limited by the maximum allowable deformation of the material under pressure and by its fabrication process. Using state-of-the-art ultra-high precision lathes, it was possible to fabricate windows with a minimum wall thickness of 0.35 mm while maintaining optical quality (they were produced in a mechanical expertise laboratory that produces optical components). Given this wall thickness, the diameter of the RHVT, and the maximum pressure in the RHVT, the maximum diameter change due to the pressure was determined to be 0.5 %. To give an estimation of uncertainties, we have assumed that the pressure gradient, the temperature gradient, and the humidity inside the RHVT had only minor influence on the refractive index of the nitrogen gas, and their influences were neglected.

The maximum astigmatism between the measurement volumes for the 514.5 and 476.5 nm wavelengths was computed to be 116 μm, which was roughly 15 % of the length of one measurement volume (650 μm). The actual length of the overlap of measurement volumes was, due to the 45° angle between the 1D and 2D probes, approximately 305 μm. This shows that the astigmatism has only minor influence on the size of the measurement volume (if properly aligned). The maximum uncertainty in the beam crossing angle was computed to be an acceptable 0.6 %. Therefore, we may assume that the beam crossing angle remains constant. To estimate the uncertainty in the measured droplet sizes, we have performed a ray tracing simulation to investigate the change in effective positioning of the sensors (the effective detector spacing). Results of this simulation show that the maximum uncertainty is 0.6 %.

Close to the wall, internal scattering of the laser light in the windows caused the signal quality to drop, making it more difficult to measure close to the wall. Because of its fabrication process, the window surface can never be perfectly smooth (the estimated surface roughness was 15 nm), causing additional scattering. Additional noise existed especially in the signals from the 1D transceiver probe, which was placed under a 45° angle (Fig. 3). It is, however, impossible to give a quantitative value of the noise and the corresponding uncertainties, because it depends on the local surface quality of the window. During the experiments, care has been taken to optimize the signal to noise (SNR) ratio to minimize the additional uncertainties due to surface imperfections.

2.4 Seeding

In this study, we used water droplets as seeding particles. The velocities of the droplets represent a good approximation of the velocity of the fluid as long as the Stokes number, $\mathrm{Stk} \ll 1$, and the centrifugal acceleration is insignificant. $\mathrm{Stk} \equiv \tau_d/\tau_f$ is the ratio of the droplet relaxation time, $\tau_d = \rho_d d_p^2/18\rho_f \nu$, and the time scale of the flow τ_f, where ρ_d and ρ_f are the density of the droplet material and the gas, respectively, d_p is the droplet diameter, ν is the kinematic viscosity of the gas.

The turbulent timescale of the flow, the Kolmogorov timescale, in the RHVT is determined to be $\tau_\kappa = \mathcal{O}(10^{-6})$ s, based on a numerical simulation (see Sect. 3.5). Using this

as timescale of the fluid, the Stokes number is $\mathrm{Stk} = \mathcal{O}(1)$ for 1 μm droplets. In this case, the constraint $\mathrm{Stk} \ll 1$ is not met and droplets are too large to follow all turbulent fluctuations. For measurements of turbulence, droplets of size $d_p = \mathcal{O}(10^{-1})\mu$m or smaller are therefore required. In this study, however, droplets are typically larger (see Sect. 3.6) and we need to limit ourselves to resolve only the larger scale velocity fluctuations.

To be able to estimate which velocity scales can be resolved, we have modeled the response of a droplet that is subjected to velocity fluctuations of its surrounding fluid by solving the equation of motion for droplets (assuming Stokes flow) taking only the drag force as relevant force (Maxey and Riley 1983)

$$\frac{\mathrm{d}U}{\mathrm{d}t} = \frac{U - V}{\tau_p} \tag{1}$$

where U is the droplet velocity. The fluid velocity oscillates in time according to $V = A\sin(\omega t)$, having a certain amplitude A and angular frequency ω. The relative droplet response amplitude is defined as $\alpha = A_p/A$, where A_p is the amplitude of the droplet motion. Ideally, $\alpha = 1$ and the droplet velocity equals that of the fluid. The corresponding timescale of the fluid is $\tau_f = 2\pi/\omega$.

Figure 4 shows the Stokes numbers and droplet response amplitudes as functions of the oscillation frequency for three droplet sizes. With increasing Stk, the droplet response amplitude decreases. For example, at a frequency of 10 kHz, a 2 μm droplet ($\mathrm{Stk} = 0.13$) has a relative response amplitude of approximately 76 %, while a 5 μm droplet ($\mathrm{Stk} = 0.84$) has a relative response amplitude of only 19 %. Consequently, droplets that have a small Stokes number follow high frequency velocity fluctuations more accurately than larger, or heavier, droplets. It will be shown later that the majority of the droplets are typically smaller than $d_p = 2$ μm and that the maximum frequency that can be measured is approximately 10 kHz. In the measurable frequency range, the Stokes numbers are $<\mathrm{Stk} \leq 0.13$.

To know the size of droplets that enter the RHVT, we have measured the droplet size distribution upstream of, and close to in the inlet. Results of this experiment show that the mean droplet size was approximately 10 μm, and the volume mean diameter (defined in sect. 3.6) was 21 μm.

Droplet concentrations in the RHVT were determined with the measured data rate, the dimensions of the measurement volume, and the velocity magnitude and were used to determine the coincidence uncertainty (i.e., the chance that there are multiple droplets in the measurement volume). We have determined that the coincidence uncertainty was 16 % at the axis and 2 % near the wall. According to the amount of water injected in the nitrogen gas, the volume fraction of droplets was $\mathcal{O}(10^{-6})$. Under the operating conditions, the gas-droplet mixture can be regarded as diluted (Elghobashi 1994) and it is highly unlikely that droplets affect each other. Therefore, we may neglect inter particle interactions.

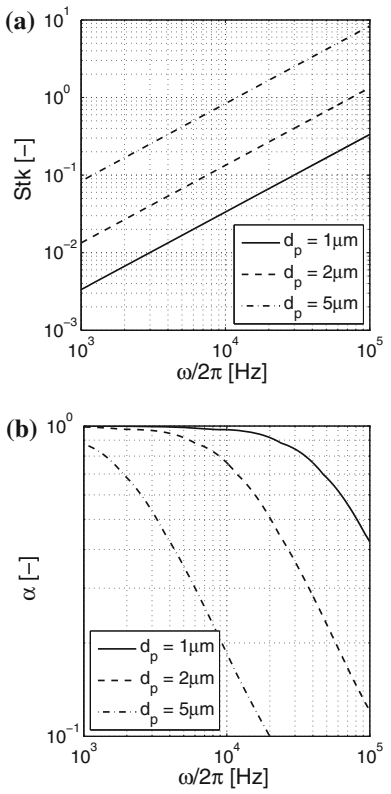

Fig. 4 **a** Stokes number, **b** relative droplet response amplitude. Both are plotted as functions of the oscillation frequency of the fluid velocity for three droplet sizes

2.5 Gas conditioning

A drawback of water droplets as seeding particles is that the water droplets evaporate in dry nitrogen gas, resulting in a depletion of seeding particles. To prevent this from happening, we humidified the nitrogen gas before it entered the RHVT.

Humidification was achieved by injecting large amounts of water droplets into the nitrogen gas stream. Droplets (<20 μm) were generated by a high pressure water pump (maximum 120 bar) that pumped water through high pressure nozzles. The nozzles were placed inside a pressure vessel (Fig. 2) that had a volume of 440 L. In the vessel, the velocity of the nitrogen was low so as to give time for the droplets to evaporate, thereby humidifying the nitrogen. The droplets that were not fully evaporated were directly injected into the RHVT. Humidifying the nitrogen has a second advantage: local (inside the vortex tube) production

of droplets. Due to the cooling effect that occurs in the vortex tube, in combination with the local pressure, the gas mixture (nitrogen and vapor) becomes locally supersaturated, causing condensation to occur.

2.6 Velocity statistics

PDPA provides samples of the velocity of individual droplets. The randomness of this sampling is influenced by, among others, the velocity magnitude (McLaughlin and Tiederman 1972) and the particle concentration (Barnett and Bentley 1974; Hoesel and Rodi 1976). High velocities magnitudes or velocities at higher particle concentrations are measured more frequently than low magnitude velocities or velocities at low particle concentration, causing a shift of the measured mean, known as the velocity bias. To minimize uncertainties caused by the bias, the particle interarrival time was used as weighting factor. This method was described by Barnett and Bentley (1974) and Hoesel and Rodi (1976) and shows to give the most accurate results (Herrin and Dutton 1993). The time averaged quantity (denoted with chevrons, $\langle\rangle$) of a velocity component, $\langle U \rangle$, was found with

$$\langle U \rangle = \frac{\sum_{i=1}^{N} U_i \Delta t_i}{\sum_{i=1}^{N} \Delta t_i} \tag{2}$$

where i is the index of the individual measurement, N is the total number of measurements, and Δt_i is the time between two individual measurements. Subscripts r, θ, and z denote the radial, swirl, and axial velocity component, respectively. The standard deviations, or rms (σ), and shear stresses (τ) were obtained in a similar way:

$$\sigma = \sqrt{\frac{\sum_{i=1}^{N} u_i^2 \Delta t_i}{\sum_{i=1}^{N} \Delta t_i}} \quad \text{and} \quad \tau = \frac{\sum_{i=1}^{N} u_i v_i \Delta t_i}{\sum_{i=1}^{N} \Delta t_i} \tag{3}$$

where $u_i = U_i - \langle U \rangle$ and $v_i = V_i - \langle V \rangle$ are the velocity fluctuations for two components of a sample with respect to their mean. The relative uncertainty in the mean values due to the finite amount of samples [see, e.g., Durst et al (1996)] is defined by $\varepsilon_m = \sigma / \langle U \rangle \sqrt{N}$ and the uncertainty in rms is $\varepsilon_\sigma = 1/\sqrt{2N}$.

2.7 Validation of the velocities measured by PDPA

The curvature of the windows, used in the experiments, introduces additional uncertainties (Sect. 2.3). To verify LDA quantities measured (here, we are mainly interested in the moments of the velocities), a classical pipe flow experiment was performed and its results were compared to results obtained from direct numerical simulation (DNS) of single-phase pipe flow (Walpot et al. 2007). The setup used in this experiment is schematically represented in Fig. 5. Pressurized nitrogen gas was fed from a nitrogen tank (N2) to a droplet generator [DG, (TSI Six Jet Atomizer, model 9306A)]. The gas/droplet mixture was injected in the pipe and passed a flow straightener (FS) and a turbulence generator (TG) to enhance the development of the flow (Den Toonder and Nieuwstadt 1997; Eggels et al 1994; Westerweel et al. 1996). The measurements took place in a transparent pipe section that was mounted near the end of the pipe. The axial velocity at the center of the pipe was matched with that obtained from the DNS for a Reynolds number of $Re = 10{,}300$ (defined as $Re = UD/\nu$ where U is the mean velocity, D the diameter of the tube, and ν the kinematic viscosity at the measured temperature in the exit of the pipe).

With PDPA, we have determined the droplet size to be 2.5 ± 1.5 μm, equivalent with a Stokes number of $\mathrm{Stk} < 0.2$, based on the shear velocity obtained from the DNS. Droplets of this size reflect the behavior of the gas and were considered as tracers.

Results from this experiment are shown in Figs. 6 and 7. The mean axial velocity as a function of the dimensionless radial coordinate, rR^{-1}, is shown in Fig. 6, where R is the

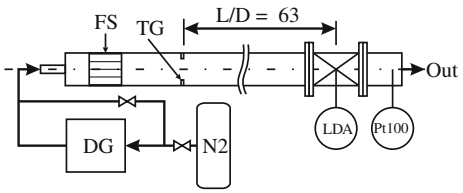

Fig. 5 Schematic overview of the experimental setup for LDA applied in a turbulent pipe flow. *FS* Flow straightener, *TG* turbulence generator, *DG* droplet generator, *N2* nitrogen supply, *Pt100* temperature sensor, and *LDA* denotes the measurement location

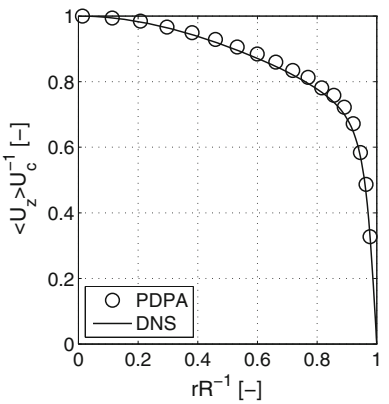

Fig. 6 Mean axial velocity for Re = 10,300 compared to DNS (Walpot et al. 2007). The symbols are the results from LDA, and the *solid lines* are the DNS results. The mean axial velocity is normalized with the *centerline* velocity U_c and plotted as a function of the dimensionless radial coordinate

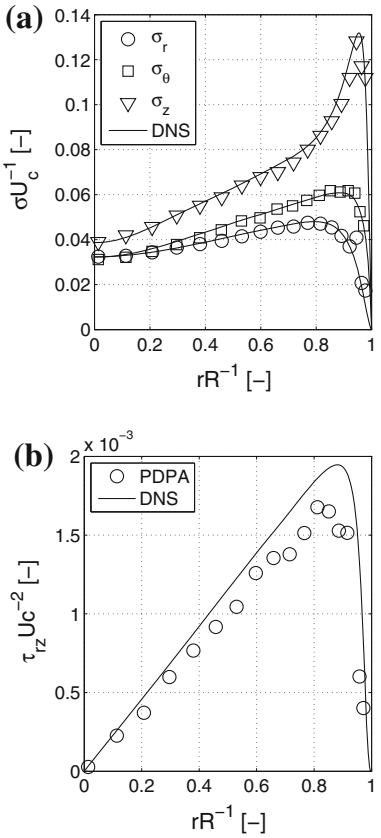

Fig. 7 **a** Standard deviation of the velocity components and **b** τ_{rz} for Re = 10,300 compared to DNS (Walpot et al. 2007). The symbols are the results from LDA, and the *solid lines* are the DNS results. The results are normalized with the *centerline* velocity U_c and plotted as a function of the dimensionless radial coordinate

radius of the pipe. The rms's of all three velocity components is shown in Fig. 7a. The results are normalized with the centerline velocity U_c. The maximum uncertainty in the mean, due to the finite amount of samples taken, was determined to be $\varepsilon_m = 1\,\%$ and the uncertainty in standard deviation $\varepsilon_\sigma = 2\,\%$, both found near the wall. Error bars are not plotted due to their negligible sizes.

For turbulent pipe flow, the only nonzero cross-component in the stress tensor is τ_{rz} (Walpot et al. 2007), which is shown in Fig. 7b. The measured shear stress is somewhat lower than predicted by the DNS, which is an indication that the flow is not fully developed; the pipe was too short for statistically fully developed pipe flow at this Reynolds number. This is confirmed by the slightly higher measured mean velocity, Fig. 6.

The means, standard deviations, and shear stresses of the velocity components for turbulent pipe flow were measured with 3D LDA. The LDA results are comparable with those of the DNS, confirming that optical abberations caused by the cylindrical window have only minor influence on the results. These results provided the confidence to carry out experiments in the RHVT.

3 Results

In this section, we present results that we have obtained from experiments in the RHVT. The experiments were performed with a nitrogen mass flow of 34.7 g/s. The number of samples taken in the experiments varied from 20,000 to 100,000. The maximum standard uncertainty was determined to be <1 % and is therefore omitted in the results. First, we show results obtained with a cold fraction of $\varepsilon = 0.35$. Later, in Sect. 3.3, we will compare these results to those for $\varepsilon = 0.65$. A frequency analysis of the velocity is presented in Sect. 3.4 and reveals the motion of the vortex core around the axis, discussed in Sect. 3.5. Due to this motion, droplets behave differently than predicted (Sect. 3.6). The radial and axial coordinates in the graphs shown in this section, r and z, respectively, are made dimensionless with the tube radius and tube length, R and L, respectively (Fig. 1).

3.1 Mean velocity

Figure 8a shows the mean swirl velocity $\langle U_\theta \rangle$ for a cold fraction of $\varepsilon = 0.35$ measured at two axial positions ($zL^{-1} = 0.03$ and $zL^{-1} = 0.07$ defined from the start of the main tube (Fig. 1). Due to viscous effects, the maximum

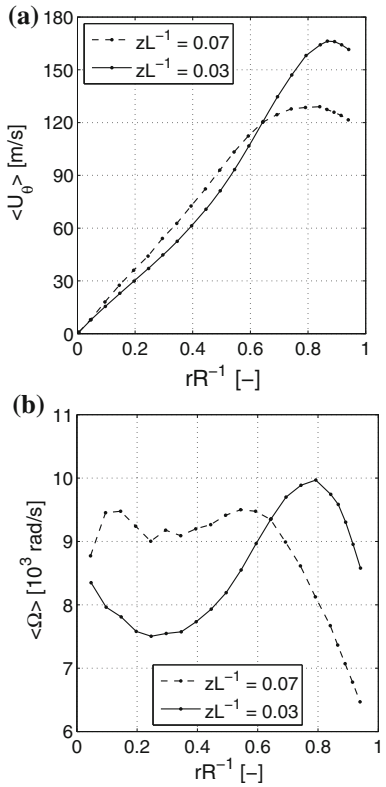

Fig. 8 **a** Swirl velocity $\langle U_\theta \rangle$ and **b** angular velocity $\langle \Omega \rangle$ as a function of the radial coordinate at two axial positions

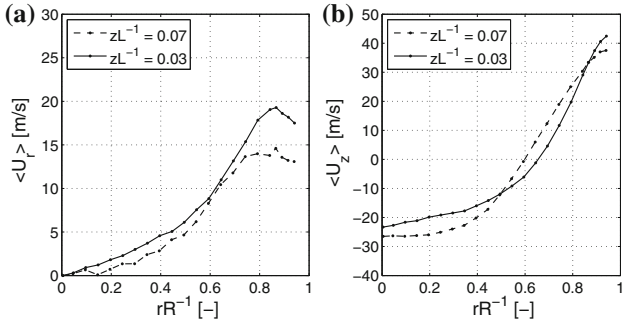

Fig. 9 **a** Radial velocity $\langle U_r \rangle$ and **b** axial velocity $\langle U_z \rangle$ as a function of the radial coordinate at two axial positions

swirl velocity decreases with increasing z, while in the core region, the vortex spins up. The spin-up is more clearly seen from the angular velocity, which is defined as $\langle \Omega \rangle = \langle U_\theta \rangle / r$, plotted in Fig. 8b. Because of conservation of angular momentum, the spin-up in the core counteracts a spin-down in the peripheral region.

Figure 9a shows the mean radial velocity $\langle U_r \rangle$ which is an order of magnitude smaller than $\langle U_\theta \rangle$. Because of the decay in swirl velocity (thus the centrifugal force), $\langle U_r \rangle$ decreases with z. The radial velocity is positive for all radii, showing that, on average, the droplets move toward the wall. Because of the small droplet size (this will be shown in Sect. 3.6), the scattered light intensity was very low, which reduced the signal to noise ratio. This effect was mainly observed in the core region, at larger z, and resulted in a lower accuracy for $\langle U_r \rangle$.

The mean axial velocity $\langle U_z \rangle$ is plotted in Fig. 9b. In the core region, the flow is directed toward the cold exit, and near the wall, the axial velocity is directed toward the hot exit. This is an indication for the presence of a secondary circulation region in the RHVT, which is also observed by, among others (Gao et al 2005; Ahlborn and Groves 1997).

3.2 Velocity fluctuations

Velocity fluctuations, especially those in radial direction, are the driving force of the energy separation process in the RHVT (Liew et al 2012). The magnitude of the velocity fluctuations is represented by the standard deviations (rms's) and the shear stresses of the velocity components.

The rms's of the three velocity components for $\varepsilon = 0.35$ is shown in Fig. 10. It shows that the trend in the magnitude of the velocity fluctuations is similar for all velocity components in the region $rR^{-1} < 0.5$.

The corresponding shear stresses are shown in Fig. 11. The shear stress components $\tau_{r\theta}$ and τ_{rz} (Fig. 11a, b, respectively) are the highest near the wall and are similar at the two axial positions. Surprisingly, $\tau_{\theta z}$ at $zL^{-1} = 0.07$ is larger than at $zL^{-1} = 0.03$, even though the fluid shows a more solid body rotation type of behavior at larger z (see Fig. 8).

Normalizing σ with the absolute velocity magnitude, we obtain the relative fluctuation intensity $I \equiv \sigma / |U|$, which is shown in Fig. 12. It shows very high values (>30 %) in the core region for all velocity components.

3.3 Comparison between different cold fractions

Previously shown results were obtained for a cold fraction of $\varepsilon = 0.35$. Now, we will compare these results to the flow characteristics at $\varepsilon = 0.65$. Here, we only compare the results at $zL^{-1} = 0.03$. $\langle U_\theta \rangle$ and the corresponding $\langle \Omega \rangle$ are shown in Fig. 13. The figures show that increasing ε leads to an increase in swirl velocity and, consequently, angular velocity. At higher cold fractions, the flow behaves even more like a solid body rotation. Therefore, the radial droplet velocity is larger for $\varepsilon = 0.65$, seen in Fig. 14a. A higher cold fraction means that more gas flows through the cold exit. Therefore, the axial velocity, shown in Fig. 14b, reaches a higher magnitude in the core region. The corresponding relative fluctuation intensities are shown in Fig. 15.

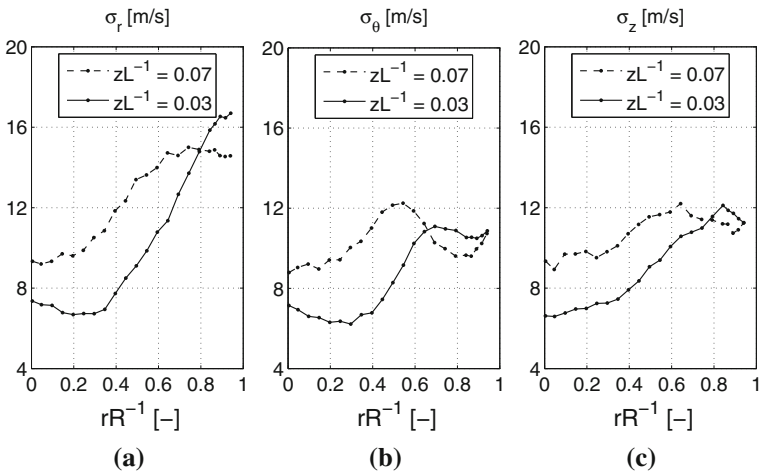

Fig. 10 Standard deviation of the velocity fluctuations as a function of the radial coordinate for two axial positions. **a** Radial component σ_r, **b** swirl component σ_θ, and **c** axial component σ_z

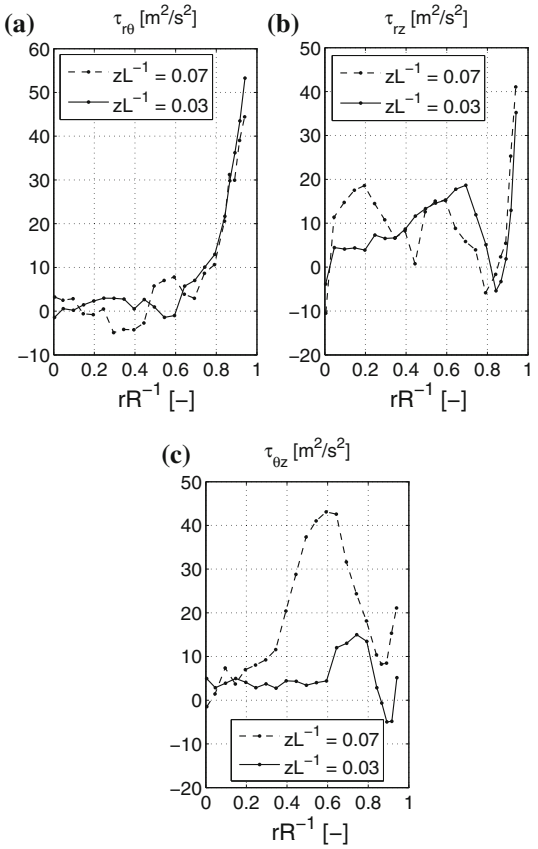

Fig. 11 Shear stresses as a function of the radial coordinate for two axial positions. **a** $\tau_{r\theta}$, **b** τ_{rz}, and **c** $\tau_{\theta\ z}$

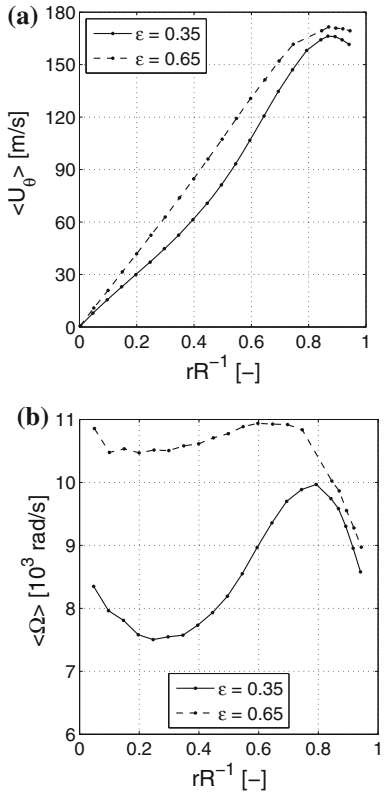

Fig. 13 **a** Swirl velocity $\langle U_\theta \rangle$ and **b** angular velocity $\langle \Omega \rangle$ as a function of the radial coordinate for two cold fractions at $zL^{-1} = 0.03$

3.4 Frequency analysis

To be able to explain the high relative fluctuation intensity in the core, the swirl velocity was measured at high data rates ($\sim$70 kHz). This allowed us to see the velocity behavior in time. One of the results is shown in Fig. 16, where U_θ at the axis is plotted as a function of time. It shows not only chaotic fluctuations, but also a high amplitude periodic behavior. The frequency spectrum of this periodic behavior contains additional information about the physics of the flow inside the RHVT. The frequency spectrum was determined with a fast Fourier transformation (FFT) of the measured velocity in time. Because of the varying time interval between two measurements, the velocity data were first interpolated onto a discrete time vector before applying the FFT.

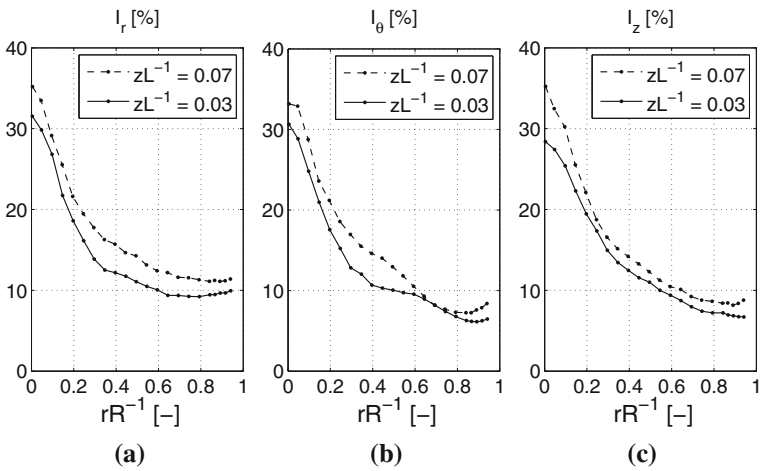

Fig. 12 Relative fluctuation intensity as a function of the radial coordinate for two axial positions. **a** Radial component I_r, **b** swirl component I_θ, and **c** axial component I_z

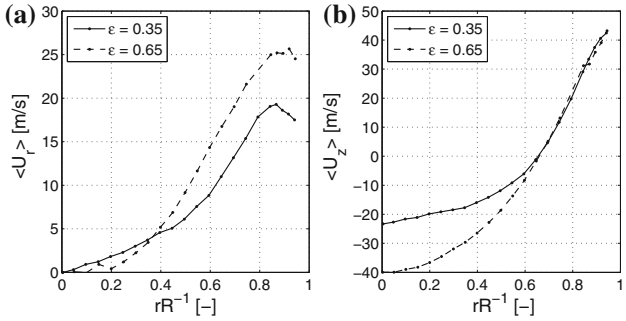

Fig. 14 **a** Radial velocity $\langle U_r \rangle$ and **b** axial velocity $\langle U_z \rangle$ as a function of the radial coordinate for two cold fractions at $zL^{-1} = 0.03$

The result of the FFT is shown in Fig. 17. In Fig. 17a, the amplitude is shown as a function of the frequency and the radial coordinate. The amplitude is normalized with the maximum amplitude (for frequencies larger than 1,000 Hz) found at the corresponding radial position. The figure shows clearly high amplitudes at distinct frequencies from which the first nonzero frequency is the fundamental frequency, f_0, which is present at all radii. As r increases, higher harmonics become visible. Remarkably, we were able to resolve up to eight harmonics (shown as the dotted lines). The radius averaged frequency amplitude is shown in Fig. 17b, clearly showing the peaks at the fundamental frequency and its higher harmonics.

The fundamental frequency of the periodic behavior was determined to be $f_0 \approx 1250$ Hz, which was approximately the same as the maximum angular frequency ($\langle \Omega \rangle_{\max} / 2\pi \approx 1260 \approx f_0$) of the main vortex. Kurosaka (1982) and Gao (2005) have found a similar agreement of the periodic behavior and the angular velocity of the main vortex.

The maximum frequency that can be determined with the FFT procedure is limited by the data rate. If the seeding concentration is homogeneous, and the signal quality constant, the data rate is a function of the velocity only. The absolute velocity magnitude increases with r (see Sect.

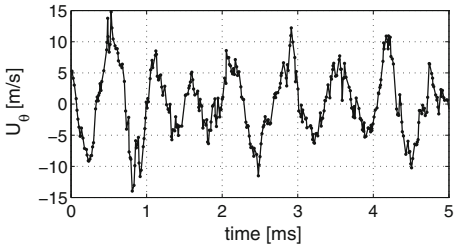

Fig. 16 A sample of the swirl velocity as a function of time, measured at $rR^{-1} = 0$ and $zL^{-1} = 0.03$

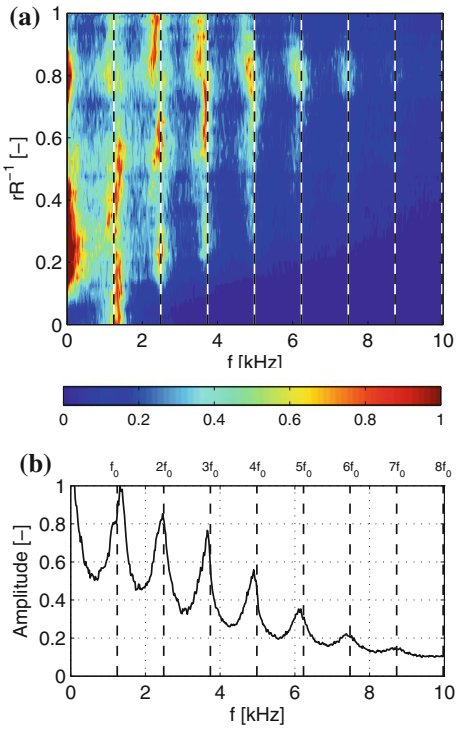

Fig. 17 The normalized frequency amplitude of U_θ measured at $zL^{-1} = 0.09$ for $\varepsilon = 0.35$. **a** Frequency amplitude as a function of the radial coordinate and the frequency, **b** radially averaged amplitude. The *dotted lines* denote the frequencies of the harmonics

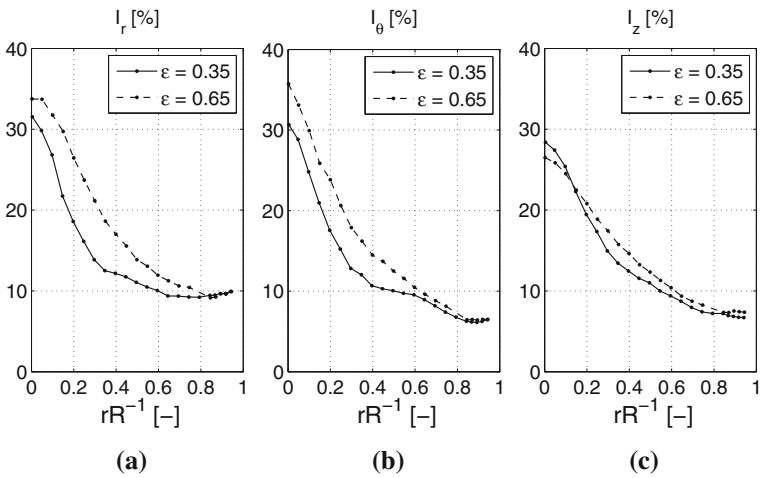

Fig. 15 Relative fluctuation intensity as a function of the radial coordinate for two cold fractions at $zL^{-1} = 0.03$. **a** Radial component I_r, **b** swirl component I_θ, and **c** axial component I_z

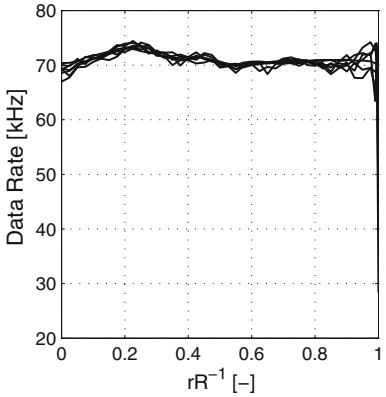

Fig. 18 Data rate as a function of the radial coordinate, measured at several positions between $0.04 \leq zL^{-1} \leq 0.09$

3.1), so taking into account the above assumptions, the data rate ideally increases toward the tube wall. This effect may increase the measured relative amplitude of higher order frequencies with r (relative to the amplitude of f_0). To see if this effect was present in our measurements, we recorded the data rate during the experiments. The data rates as a function of r for several axial positions are shown in Fig. 18. The figure shows that the actual data rate remains approximately constant, what indicates that the seeding concentration decreases with r. From this, we may conclude that the results shown in Fig. 17 are not influenced by the data rate, and that it is safe to neglect this effect.

If we take the fundamental frequency, f_0, and plot its normalized amplitude as a function of r and z (Fig. 19a), we see that it has the highest amplitude in the core region and reappears at $rR^{-1} \approx 0.5$. Interesting is to see that the amplitude of f_0 increases with z. The second harmonic, $2f_0$, is shown in Fig. 19b, which shows that the amplitude of this frequency is very low at the axis.

The frequency analysis was also applied to U_z, obtained from a different experiment. In this experiment, the data rate was approximately 30 kHz, and the result is shown in Fig. 20. The figure shows that the fundamental frequency is also present in this velocity component. Because of the similarity in the three rms's of the velocity components (Fig. 10), we expect to find this as well in U_r. Unfortunately, it was impossible to have a sufficiently high enough data rate for U_r to proof this.

3.5 Vortex wobbling

The existence of the high amplitude periodic behavior can be explained by the following. The axis of the main vortex, that is, the vortex filament, is typically not located exactly *at* the axis of the tube but is located off-axis. Due to the off-axis alignment and its confinement, the vortex filament rotates *around* the RHVT axis, causing a wobbling of the

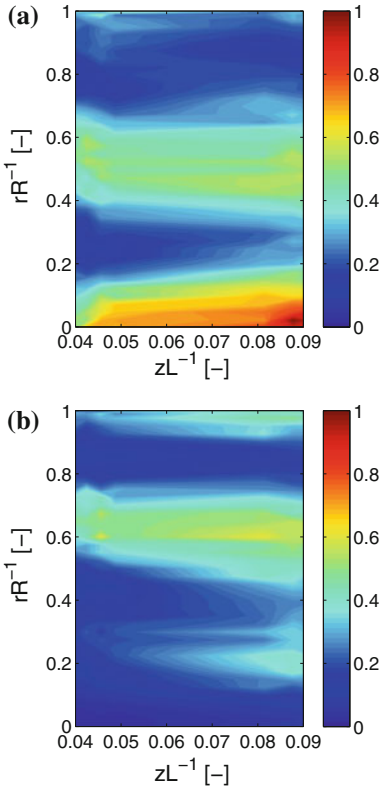

Fig. 19 The normalized frequency amplitude for U_θ as a function of the radial and axial coordinates. **a** Fundamental frequency $f_0 \pm 40$Hz, **b** second harmonic $2f_0 \pm 40$Hz. The amplitudes are normalized with the maximum value found for f_0

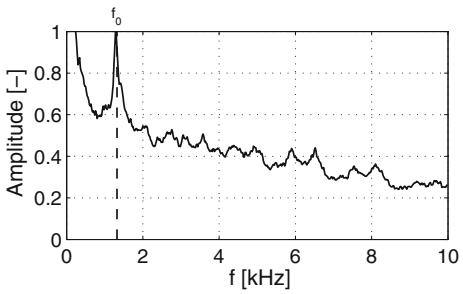

Fig. 20 The normalized frequency amplitude of U_z, averaged in radial direction, measured at $zL^{-1} = 0.04$. The *dotted line* denotes the fundamental frequency

vortex. This motion of a vortex filament in a closed circular domain was already described by Lamb (1932, §155) and, more recently, by Fukumoto and Okulov (2005) and IJzermans et al. (2007). In the presence of a nonzero U_z, the vortex filament forms a helical type of shape, schematically represented in Fig. 21. Let point A be an instantaneous location of the vortex filament, then this point follows a circular pattern, which has an angular velocity $\Omega_2 = \dot{\phi}$, around the tube axis as time progresses (dotted lines). If the radius of the circular pattern is much

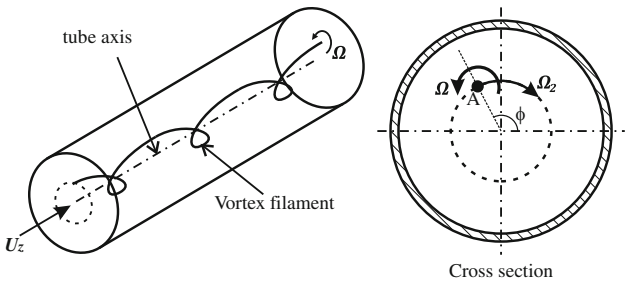

Fig. 21 A confined vortex filament rotating around a tube axis. At a certain time, the center of the vortex filament is located in point A. The vortex filament follows a circular pattern (*dotted line*) around the tube axis as time progresses. Ω is the angular velocity of the vortex filament, $\Omega_2 = \dot{\varphi}$ is the angular velocity of the rotation around the axis, and φ is the angular position

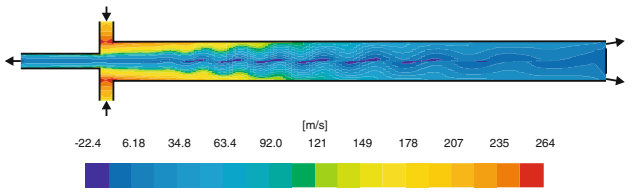

Fig. 22 Contour plot of the absolute swirl velocity obtained from numerical simulation

smaller than the tube radius, we can make the approximation $\Omega_2 \approx \langle\Omega\rangle_{\max}$. This explains why $f_0 \approx \langle\Omega\rangle_{\max}/2\pi$.

We have numerically computed the flow field in the RHVT with Fluent™ [compressible RANS ($k-\epsilon$ model), steady state, coupled pressure-based solver] to show the vortex wobbling. The computational domain for a vortex tube, which has a inner diameter of 40 mm and a length of 500 mm, contained 2.4 million nodes. The simulation was 3D to be able to capture non-axisymmetric behavior, for example, vortex wobbling. The results were obtained using the following boundary conditions: inlet mass flow 69.8 g/s; plenum pressure 4.70 bar; inlet temperature 295 K; $\varepsilon = 0.35$. One of the results is shown in Fig. 22, which shows the absolute swirl velocity. Although it is a result from a steady state simulation, it clearly shows non-axisymmetric behavior of the vortex. It shows that this type of flow is naturally unsteady.

To see how large the contribution of velocity fluctuations that are caused by the vortex wobbling is to the rms's, the main and higher order frequencies were subtracted from the velocity signal. To do so, the velocity signal passed a high pass filter that had a cutoff frequency of 10 kHz (based on the frequency of the eighth harmonic, $8f_0$). This filtered velocity was then subtracted from the initial signal. What remained were the velocity fluctuations that were superimposed onto the wobbling motion of the vortex, that is, the turbulence. The rms of this filtered signal, σ_f, was determined and compared to σ (the rms of the original velocity). The contribution of the wobbling, ψ, was found with

$$\psi = \left(1 - \frac{\sigma_f}{\sigma}\right) \times 100\,\% \tag{4}$$

If $\psi = 100$ %, all the velocity fluctuations are due to the wobbling, and if $\psi = 0$ %, all the velocity fluctuations are due to turbulence.

In Fig. 23a, we show σ and σ_f as a function of the radial coordinate. The corresponding values for ψ_θ are shown in Fig. 23b. This figure explains why the relative fluctuation intensity is so high at the axis and decreases toward the wall: Approximately 75 % of the measured fluctuation intensity at the axis, 20 % near the wall is caused by the vortex wobbling. The turbulence intensity $T = I(1 - \psi)$ is for all radii determined to be <10 %.

3.6 Droplet behavior

Because of the positioning of the 1D probe (Fig. 3), the signal intensity of the third component is low compared to the other two components. The FSA4000 processor discards bad quality signals, which are mostly from the smallest droplets. To prevent a size bias in the measured

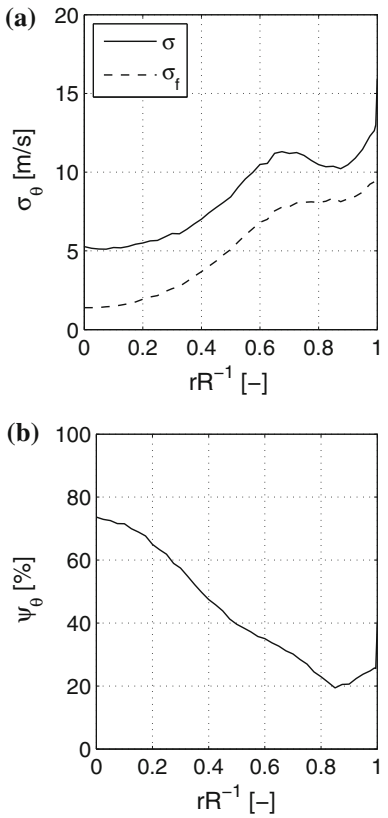

Fig. 23 **a** The original (σ) and filtered (σ_f) standard deviations of U_θ. **b** The contribution of the vortex wobbling in σ as a function of the radial coordinate, measured at $zL^{-1} = 0.04$

size distributions, the droplet size distributions were measured by using the 514.5 nm wavelength and the RV-probe (see Fig. 3), which gave the highest quality signals.

Two measured droplet size distributions are shown in Fig. 24. In this figure, we show normalized droplet size distribution functions (nPDF) measured at two radial positions in the RHVT. Because the minimum droplet size that can be measured with PDPA is 0.5 μm, there is no size data available for droplets smaller than 0.5 μm. Fig. 24a shows the nPDF at $rR^{-1} = 0$, and Fig. 24b shows the nPDF near the wall at $rR^{-1} = 0.95$. The cumulative size distribution functions (CDF) are shown as the solid lines in the figures and show that 95 % of the droplets measured are smaller than $d_p < 2$ μm at the axis and $d_p < 3$ μm near the wall.

The volume distributions at the axis and near the wall are shown in Fig. 25a, b, respectively. The corresponding cumulative distributions (solid lines in the figures) show that about 95 % of the liquid water is in the form of droplets that are smaller than 4 μm.

There is not only a change in droplet size in radial direction, but also in axial direction. Figure 26 shows both the mean and the volume mean diameter as a function of rR^{-1} for different values of zL^{-1}. The volume mean $\langle d_p \rangle_v$ was computed according to

$$\langle d_p \rangle_v = \left(\frac{\sum_{i=1}^{N} d_p^3}{N} \right)^{1/3} \tag{5}$$

where we have adopted N and i from Sect. 2.6. The results show that the largest droplets can be found near the wall or close to the entrance and that the droplets size decreases with increasing z.

The radial velocity of the droplets is an important parameter for the design the RHVT separator. This velocity can be used to predict the location in the RHVT at which the droplets hit the wall and form an—easy to separate—liquid film. If the swirl velocity of the fluid is known, the radial velocity of the droplets can be computed from a balance between the centrifugal force and the drag force (Bird et al. 2007). For small droplets, the Stokes drag force can be applied

$$F_d = 3\pi\rho_f \nu d_p (U - V) \tag{6}$$

where U and V are the droplet and fluid velocity, respectively. The above equation is valid for a droplet Reynolds number $Re_d = d_p|U - V|/\nu < 1$. To be able to

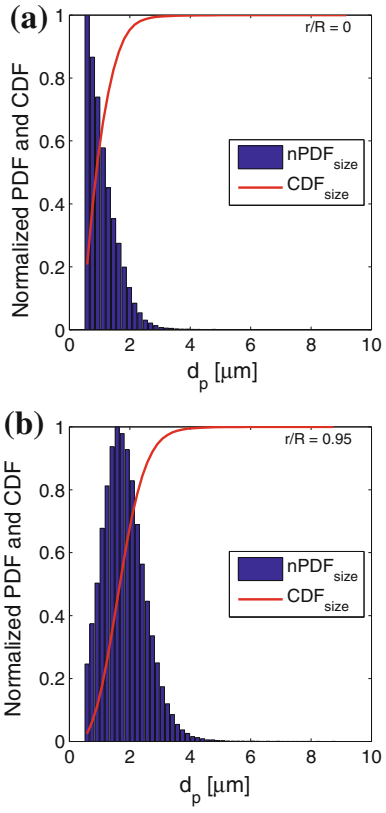

Fig. 24 Normalized size distributions (nPDF) and cumulative distributions functions (CDF) based on droplet size at $zL^{-1} = 0.04$. **a** $rR^{-1} = 0$ and **b** $rR^{-1} = 0.95$

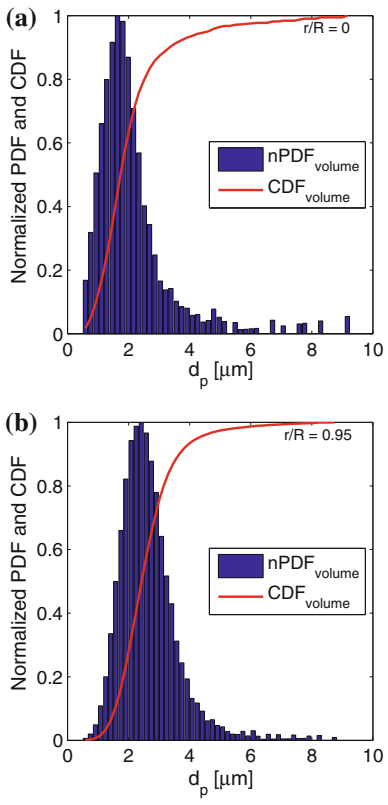

Fig. 25 Normalized size distributions (nPDF) and cumulative distributions functions (CDF) based on droplet volume at $zL^{-1} = 0.04$. **a** $rR^{-1} = 0$ and **b** $rR^{-1} = 0.95$

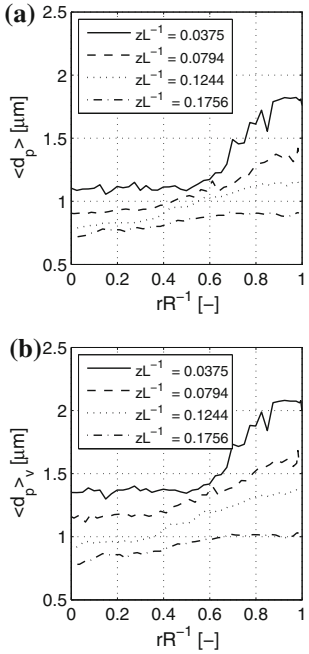

Fig. 26 **a** Mean droplet diameter $\langle d_p \rangle$ and **b** volume mean diameter $\langle d_p \rangle_v$ as a function of rR^{-1} and zL^{-1}

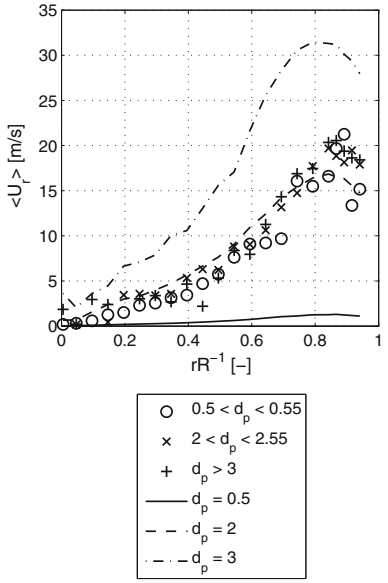

Fig. 27 Radial velocity as function of the radial coordinate for droplet size intervals $0.5 < d_p < 0.55$, $2 < d_p < 2.05$, and $d_p > 3$ μm compared to results of Eq. (7) for $d_p = 0.5$, $d_p = 2$, and $d_p = 3$ μm. *Symbols* experimental results, *lines* Eq. (7) by using the measured $\langle U_\theta \rangle$

take into account the fact that the Reynolds number may exceed one, we use the correlation $C = 1 + 0.15Re_d^{0.687}$, which is valid for $Re_d < 800$ and is the ratio of the actual drag force to the Stokes drag force (Schiller and Naumann 1933). By equating the drag force to the centrifugal force $F_c \approx \rho_p \frac{\pi}{6} d_p^3 \Omega^2 r$, we find the terminal (radial) velocity of droplets with respect to the fluid, that is, the radial drift velocity $U_{\text{drift}} = U - V$. Using the definition of the particle relaxation time τ_d (Sect. 2.4), we obtain

$$U_{\text{drift}} = \Omega^2 r \frac{\tau_d}{C} \tag{7}$$

Because τ_d depends quadratically on the droplet size, we would expect that the measured radial droplet velocity is higher for large droplets than for small droplets.

Figure 27 shows the radial velocity for three droplet size intervals. The measured values are shown with symbols for $0.5 < d_p < 0.55$, $2 < d_p < 2.05$, and $d_p > 3$ μm. For convenience, the theoretical predictions according to Eq. (7) for droplet sizes $d_p = 0.5$, $d_p = 2$, and $d_p = 3$ μm are added. According to Eq. (7), the radial velocity for the larger droplets should be higher than that of the smaller droplets. The figure, however, shows that this is not the case. The smallest droplets have a significantly higher radial velocity than predicted by Eq. (7), while the larger droplets have a lower velocity. All droplet size intervals behave approximately the same as the $d_p = 2$ μm droplets.

Scatter plots of the instantaneous velocity fluctuations (defined in Sect. 2.6) as functions of the measured droplet size are shown in Figs. 28, 29 and 30 for the three velocity components. We have added bin averaged radial velocities to show the velocity-size dependence. The top graphs show the velocity fluctuations of droplets at the axis, while the bottom graphs show the velocity fluctuations close to the wall. The bin averaged velocity shows that in both locations and for all velocity components, there is no noticeable correlation between droplet size and droplet velocity (only the swirl velocity seems to increase slightly with the droplet size).

That the droplet size and velocity are uncorrelated can be explained by taking a closer look into the behavior of

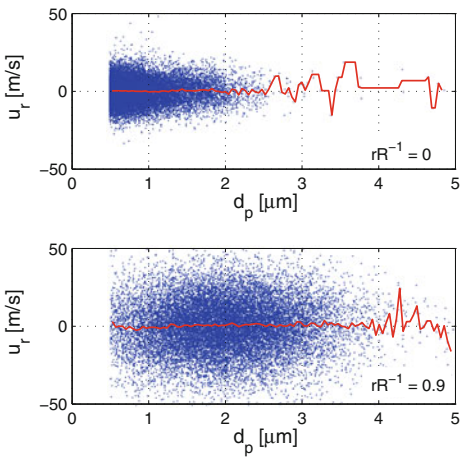

Fig. 28 Instantaneous radial velocity fluctuations of droplets as a function of the droplet size at the axis (*top*) and near the wall (*bottom*). The *solid lines* are the bin average for a bin size of 0.05 μm

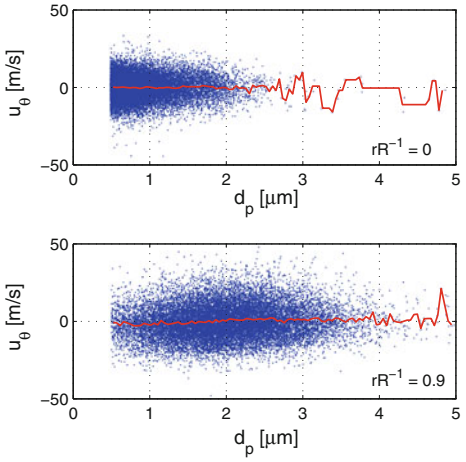

Fig. 29 Instantaneous swirl velocity fluctuations of droplets as a function of the droplet size at the axis (*top*) and near the wall (*bottom*). The *solid lines* are the bin average for a bin size of 0.05 μm

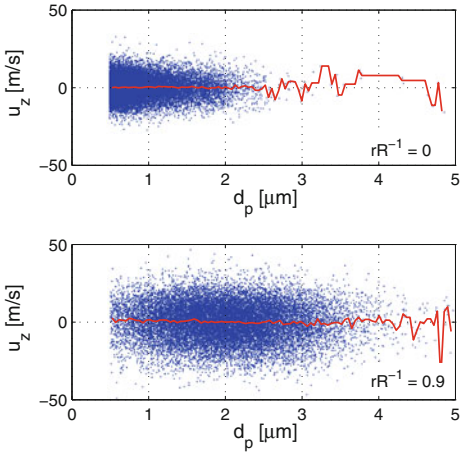

Fig. 30 Instantaneous axial velocity fluctuations of droplets as a function of the droplet size at the axis (*top*) and near the wall (*bottom*). The *solid lines* are the bin average for a bin size of 0.05 μm

the vortex filament, as described in Sect. 3.2. IJzermans et al. (2007) computed the velocity field and the motion of a vortex filament that was positioned off-axis in a cylindrical tube (Fig. 21). They have shown that there exists a nonzero radial velocity component due to asymmetry of the vortex. The additional (drag) force, caused by this velocity component, reduces the effect of the centrifugal force. If this force is larger than the centrifugal force, the droplet size becomes of minor importance for the drift velocity. This might be an undesired phenomenon for the efficiency at which droplets can be separated. Kuerten et al. (2007) and Van Esch and Kuerten (2008) also performed numerical simulations of particles in a asymmetric vortex and showed that the separation efficiency decreases compared to an axisymmetric vortex.

From the previous explanations, the following question is raised: Why do the size distributions change with r, as shown in Figs. 24 and 26, while the radial velocities are equal for all droplet sizes? After all, if the radial velocity is independent of the droplet size, the size distributions should be equal for all radii.

A possible explanation for the change in size distributions is that the droplet size varies in the entrance region due to the way of injecting the droplets into the vortex chamber. In this region, there is no wobbling motion of the vortex and the centrifugal force is more important. Because the gas and the droplets are injected via the entrances of the RHVT, in combination with the centrifugal force, it is very plausible that larger droplets are found near the wall. In the peripheral region, the axial velocity is positive and the (relative large) droplets move toward the hot end. In the core region, the axial velocity is negative, and droplets, which are traveling back from the hot end toward the cold exit, have smaller sizes. These droplets are smaller because they partly evaporate during their travel. A measurement at one specific axial position shows, consequently, smaller droplets in the core and larger droplets near the wall.

On top of this, there is a second effect, which is caused by the pressure and temperature distribution inside the RHVT. Due to the centrifugal force, the pressure increases with r (Ahlborn et al. 1994; Gao 2005). For a certain mass fraction of water vapor in the gas, the humidity varies with the pressure and temperature (Liew et al. 2011). If Θ is the molar concentration of water vapor in the gas, the relative humidity RH is

$$\mathrm{RH} = \frac{p\Theta}{p_{\mathrm{sat}}(T)} \times 100\,\% \tag{8}$$

where $p_{\mathrm{sat}}(T)$ is the saturation vapor pressure at temperature T, and p is the pressure of the gas mixture. Assuming a constant Θ (defined for RH = 99 % humidity under plenum conditions), and using the pressure and temperature obtained from the numerical simulation (see Sect. 3.5), we obtain the local relative humidity in the RHVT (if no spontaneous condensation would occur).

Figure 31 shows the local relative humidity in the RHVT. In the region near the vortex chamber, the gas mixture is supersaturated (RH $>$ 1 00 %). In this region, droplets grow due to condensation. Here, the humidity increases with r due to an increasing pressure. Therefore, droplets that move with positive U_r grow due to condensation, what results in larger droplets near the wall than in the core region. Note that in the result shown in Fig. 31, evaporation and condensation are not taken into account.

On the other hand, the swirl velocity decreases and the temperature increases with z, resulting in lower humidities. Consequently, droplets evaporate at larger z. Both the droplet size increase with r and the decrease with z are

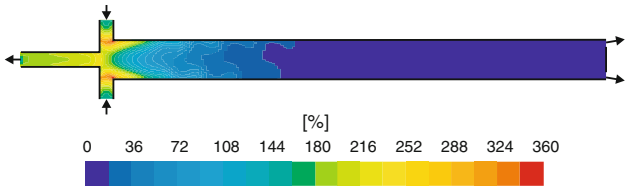

Fig. 31 Contour plot of the relative humidity obtained from numerical simulation

clearly shown in Fig. 26. At $zL^{-1} \approx 0.2$; the gas was undersaturated and droplets evaporated. PDPA measurements were, therefore, not possible for larger z.

4 Conclusions

We have performed PDPA experiments in the near entrance region of the RHVT to give insight into the behavior of water droplets in the RHVT. The PDPA method provided detailed results, related to the three dimensional velocity field, its statistical properties, and droplet properties.

Three velocity components have been measured. Increasing the cold fraction also leads to an increase in maximum swirl velocity and a higher axial velocity toward the cold exit. At larger axial positions, the angular velocity in the core increases, showing a spin-up of the vortex core. The mean radial velocity increases with r and decreases with z.

The rms's of the velocity fluctuations is similar to each other in the core region. The relative fluctuation intensity increases not only with z, but also with ε and is very high (>30 %) at the axis and decreases toward the wall. To explain the high intensity, we analyzed the frequencies of the velocity signal. There is a high amplitude fundamental frequency that is strongly correlated to the angular velocity. This frequency has the highest amplitude at the axis of the RHVT. With increasing r, higher orders (up to the eighth order) frequencies were found.

The fundamental frequency is not only found in the swirl velocity component, but also in the axial velocity component. Because of the similarity in the standard deviations of the velocity components, it is expected to find the same fundamental frequency in the radial velocity component.

The strong correlation of the fundamental frequency to the angular velocity is due to the wobbling of the (helical) vortex around the tube axis. By subtracting the fundamental and higher order frequencies from the velocity signal, we have determined that 75 % of the magnitude of the fluctuations at the axis, and 20 % near the wall is caused by the wobbling of the vortex. According to this, the turbulence intensity is <10 %.

The droplet sizes were determined with PDPA. Results show that the droplets in the RHVT are very small, typically $d_p < 5$ μm (the majority is smaller than $d_p = 2$ μm). The largest droplets can be found near the entrances and the tube wall of the RHVT, where the local humidity is the highest; smaller droplets were found at the axis, or at larger z. It was expected that larger droplets would have a higher radial velocity than smaller droplets due to the larger centrifugal force. The results show, unexpected, that there is no correlation between droplet size and U_r.

Due to the wobbling of the vortex axis, there is a non-zero radial velocity component. The drag force, resulting from this velocity, reduces the effect of the centrifugal force on the radial droplet velocity. Because of this, the droplet size has a minor influence on U_r.

The variation of droplet sizes inside the RHVT is mainly caused by the combination of two effects. First, the droplet size varies in the inlet region (vortex chamber) due to the centrifugal force and the axial velocity. Secondly, the humidity in the RHVT varies with the pressure and temperature and local condensation or evaporation causes the droplet size distributions to change.

Acknowledgments The authors would like to thank R. Hagmeijer for his useful comments regarding vortex wobbling and H.B.M. Manders and J.M. van der Veen for their technical support. This research is supported by the Dutch Technology Foundation STW, which is the applied science division of NWO, and the Technology Programme of the Ministry of Economic Affairs.

References

Ahlborn BK, Groves S (1997) Secondary flow in a vortex tube. Fluid Dyn Res 21:73–86

Ahlborn BK, Keller JU, Staudt R, Treitz G, Rebhan E (1994) Limits of temperature separation in a vortex tube. J Phys D Appl Phys 27:480–488

AirTx (2012) http://www.airtx.com/vortex-tubes

Albrecht HE (2003) Laser doppler and phase doppler measurement techniques. Springer, Berlin

Aljuwayhel NF, Nellis GF, Klein SA (2005) Parametric and internal study of the vortex tube using a CDF model. Int J Refrig 28:442–450

Bachalo WD, Houser MJ (1984) Phase/doppler spray analyzer for simulataneous measurements of drop size and velocity distributions. Opt Eng 1:428–444

Barnett DO, Bentley HT (1974) Statistical bias of individual realization laser velocimeters. Proc Second Int Workshop Laser Velocim 1:428–444

Bird BR, Stewart WE, Lightfoot EN (2007) Transport phenomena, 2nd edn. Wiley, Hoboken, NJ

Deissler RG, Perlmutter M (1960) Analysis of the flow and energy separation in a turbulent vortex. Int J Heat Mass Trans 1: 173–191

Den Toonder JMJ, Nieuwstadt FTM (1997) Reynolds number effects in a turbulent pipe flow for low to moderate Re. Phys Fluids 9(11):3398–3409

Durst F, Kikura H, Lekakis I, Jovanovic J, Ye Q (1996) Wall shear stress determination from near-wall mean velocity data in turbulent pipe and channel flows. Exp Fluids 20:417–428

Eggels JGM, Unger F, Weiss MH, Westerweel J, Adrian RJ, Friedrich R, Nieuwstadt FTM (1994) Fully developed turbulent pipe flow, a comparison between direct numerical simulation and experiment. J Fluid Mech 268:175–209

Eiamsa-ard S, Promvonge P (2008) Review of Ranque–Hilsch effects in vortex tubes. Renew Sust Energ Rev 12:1822–1842

Elghobashi S (1994) On predicting particle-laden turbulent flows. Appl Sci Res 52:309–329

Exair (2012) http://www.exair.com

Fukumoto Y, Okulov VL (2005) The velocity field induced by a helical vortex tube. Phys Fluids 17(10):107101

Gao CM (2005) Experimental study on the Ranque–Hilsch vortex tube. PhD thesis, Eindhoven University of Technology

Gao CM, Bosschaart KJ, Zeegers JCH, de Waele ATM (2005) Experimental study on a simple Ranque–Hilsch vortex tube. Cryogenics 45:173–183

Gutsol A (1997) The Ranque effect. Phys Uspeki 40(6):639–658

Herrin JL, Dutton JC (1993) An investigation of LDV velocity bias correction techniques for high speed separated flows. Exp Fluids 14:354–363

Hilsch R (1947) The use of the expansion of gases in a centrifugal field as cooling process. Rev Sci Instr 18:108–113

Hoesel W, Rodi W (1976) New biasing elimination method for laser doppler velocimeter counter processing. Rev Sci Instr 48(7):910–919

IJzermans RHA, Hagmeijer R, van Langen P J (2007) Accumulation of heavy particles around a helical vortex filament. Phys Fluids 19:107102

ITW-Vortec (2012) http://www.vortec.nl

Kuerten JGM, van Esch BPM, van Kemenade HP, Brouwers JJH (2007) The effect of turbulence on the efficiency of the rotational phase separator. Int J Heat Fluid Fl 28:630–637

Kurosaka M (1982) Acoustic streaming in swirling flow and the Ranque Hilsch effect. J Fluid Mech 124:139–172

Lamb H (1932) Hydrodynamics, 6th edn. Cambridge University Press, Cambridge

Liew R, Zeegers JCH, Kuerten JGM, Michalek WR (2011) Droplet behaviour in a Ranque–Hilsch vortex tube. J Phys Conf Ser 318:052013

Liew R, Zeegers JCH, Kuerten JGM, Michalek WR (2012) Maxwell's Demon in the Ranque–Hilsch Vortex Tube. Phys Rev Lett 109:054503

Maxey MR, Riley JJ (1983) Equation of motion for a small rigid sphere in a nonuniform flow. Phys Fluids 26:883–839

McLaughlin DK, Tiederman WG (1972) Biasing correction for individual realization of laser anemometer measurements in turbulent flows. Phys Fluids 16(12):2082–2088

Nimbalkar SU, Muller MR (2009) An experimental investigation of the optimum geometry for the cold end orifice. Appl Therm Eng 29:509–514

Ranque GJ (1933) Experiences sur la detente avec production simultanees d'un echappement d'air chaud et echappement d'air froid. J Phys Radium 7(4):112–4–S–115

Schiller L, Naumann AZ (1933) über die grundlegenden berechnungen bei der schwerkraftaufbereitung. Ver Deut Ing 77:318–320

Takahama H, Yokosawa H (1981) Energy separation in vortex tubes with a divergent chamber. J Heat Trans 103(2):196–203

TSI Inc. (2012) http://www.tsi.com

Van Esch BPM, Kuerten JGM (2008) DNS of the flow of particles in rotating pipe flow. J Turbul 9(4):1–17

Walpot RJE, van der Geld CWM, Kuerten JGM (2007) Determination of the coeffcients of langevin models for inhomogeneous turbulent flows by 3D PTV and DNS. Phys Fluids 19:045,102

Westerweel J, Draad AA, Hoeven JGT, Oord J (1996) Measurement of fully-developed turbulent pipe flow with digital particle image velocimetry. Exp Fluids 20:165–177

Zhang Z (2004) Optical guidelines and signal quality for LDA applications in circular pipes. Exp Fluids 37:29–39

Zhang Z, Eisele K (1996) The effect of astigmatism due to beam refractions on the formation of the measurement volume in LDA measurements. Exp Fluids 20:466–471

Zhang Z, Eisele K (1998) Further considerations of the astigmatism error associated with off-axis alignment of an LDA-probe. Exp Fluids 24:83–89